Quantitative 3D Magnetic Resonance Elastography: Comparison With Dynamic Mechanical Analysis

Shivaram P. Arunachalam,[1]* Phillip J. Rossman,[1] Arvin Arani,[1] David S. Lake,[2] Kevin J. Glaser,[1] Joshua D. Trzasko,[1] Armando Manduca,[2] Kiaran P. McGee,[1] Richard L. Ehman,[1] and Philip A. Araoz[1]

Purpose: Magnetic resonance elastography (MRE) is a rapidly growing noninvasive imaging technique for measuring tissue mechanical properties in vivo. Previous studies have compared two-dimensional MRE measurements with material properties from dynamic mechanical analysis (DMA) devices that were limited in frequency range. Advanced DMA technology now allows broad frequency range testing, and three-dimensional (3D) MRE is increasingly common. The purpose of this study was to compare 3D MRE stiffness measurements with those of DMA over a wide range of frequencies and shear stiffnesses.

Methods: 3D MRE and DMA were performed on eight different polyvinyl chloride samples over 20–205 Hz with stiffness between 3 and 23 kPa. Driving frequencies were chosen to create 1.1, 2.2, 3.3, 4.4, 5.5, and 6.6 effective wavelengths across the diameter of the cylindrical phantoms. Wave images were analyzed using direct inversion and local frequency estimation algorithm with the curl operator and compared with DMA measurements at each corresponding frequency. Samples with sufficient spatial resolution and with an octahedral shear strain signal-to-noise ratio > 3 were compared.

Results: Consistency between the two techniques was measured with the intraclass correlation coefficient (ICC) and was excellent with an overall ICC of 0.99.

Conclusions: 3D MRE and DMA showed excellent consistency over a wide range of frequencies and stiffnesses. **Magn Reson Med 77:1184–1192, 2017.** © **2016 The Authors Magnetic Resonance in Medicine published by Wiley Periodicals, Inc. on behalf of International Society for Magnetic Resonance in Medicine. This is an open access article under the terms of the Creative Commons Attribution-NonCommercial-NoDerivs License, which permits use and distribution in any medium, provided the original work is properly cited, the use is non-commercial and no modifications or adaptations are made.**

Key words: magnetic resonance elastography; dynamic mechanical analysis; shear modulus; storage modulus; loss modulus

INTRODUCTION

Magnetic resonance elastography (MRE) is a rapidly growing noninvasive imaging technique that can measure soft tissue stiffness in vivo (1,2). In MRE, tissues are interrogated with shear waves from an external mechanical vibration source. The propagating shear waves are imaged using a modified phase contrast MRI pulse sequence. The wave displacement data are converted to stiffness maps through mathematical techniques, collectively called "inversions," of which the most widely used are direct inversion (DI) of the Helmholtz equation and local frequency estimation (LFE) (3)

Validation of MRE stiffness measurements has typically been done with mechanical testing of custom-made phantoms. However, published studies to date have had several limitations. First, the mechanical test most analogous to MRE and reported most often in the literature is dynamic mechanical analysis (DMA), which to date has had unreliable performance at frequencies over 100 Hz (4,5). As a result, DMA validation of MRE has generally been performed with comparisons that overlap only over narrow frequency ranges, and comparisons at frequencies over 100 Hz have often been performed by extrapolating DMA results to higher frequencies (6–11). Second, phantom validation has generally involved two-dimensional (2D) acquisitions, and without processing with the curl operator. Three-dimensional (3D) MRE acquisitions are increasingly common, and many groups now apply the curl operator to remove the longitudinal component of the displacement field (12,13), although at the expense of noise amplification (4,14). A comprehensive phantom study that compares the accuracy of such 3D quantitative MRE stiffness measurements over a wide range of frequencies and stiffness values by direct comparison with mechanical testing is therefore needed.

The purpose of this study was to evaluate the accuracy of quantitative 3D MRE using curl processing with the 3D DI and LFE algorithms over a range of different frequencies in phantoms with different stiffness values using a commercially available DMA instrument, which can perform over a wide range of vibration frequencies from 1 to 2000 Hz as a reference standard.

[1]Department of Radiology, Mayo Clinic, Rochester, Minnesota, USA.

[2]Department of Physiology and Biomedical Engineering, Mayo Clinic, Rochester, Minnesota, USA.

Grant sponsor: National Institutes of Health; Grant numbers: 5R01HL115144 and EB001981.

*Correspondence to: Shivaram Poigai Arunachalam, M.S., M.P.H., Department of Radiology, Mayo Clinic, 200 First Street SW, Rochester, MN 55905. E-mail: poigaiarunachalam.shivaram@mayo.edu; Twitter: @ShivaramPoigai

Received 22 September 2015; revised 11 January 2016; accepted 17 February 2016

DOI 10.1002/mrm.26207
Published online 26 March 2016 in Wiley Online Library (wileyonlinelibrary.com).

© 2016 The Authors Magnetic Resonance in Medicine published by Wiley Periodicals, Inc. on behalf of International Society for Magnetic Resonance in Medicine. This is an open access article under the terms of the Creative Commons Attribution-NonCommercial-NoDerivs License, which permits use and distribution in any medium, provided the original work is properly cited, the use is non-commercial and no modifications or adaptations are made.

METHODS

Preparation of Eight Polyvinyl Chloride Cylindrical Phantoms and Associated DMA Samples

Eight different polyvinyl chloride (PVC) (LureCraft Inc, Orland, Indiana, USA) mixtures of different stiffnesses were used to study the accuracy of 3D MRE with curl compared with DMA. For each mixture of PVC, one cylindrical phantom of diameter 15.25 cm and height 12.5 cm was created for MRE imaging, and two smaller cylindrical tubes of inner diameter 0.9 cm and height 4.5 cm were made for DMA testing. The eight PVC mixtures were made with different volume ratios of PVC to softening agent (Lure Craft, Inc); for example, PVC 60-40 implies that it is a mixture of 60% PVC and 40% softener, and so forth. The eight samples include PVC 50-50, PVC 60-40, PVC 70-30, PVC 75-25, PVC 80-20, PVC 85-15, PVC 90-10, and PVC 95-05. Each mixture was heated to between 150°C and 175°C in a glass container with constant stirring and then poured into one cylindrical phantom mold for MRE imaging and two small cylindrical tubes for DMA testing. The samples were air-sealed in a plastic bag. All samples were allowed to cure for more than 90 days to ensure stabilization of the mechanical properties of the material. All measurements were performed at room temperature (~25°C).

DMA

For each of the eight mixtures, a new approach for DMA was performed on the two small cylindrical tube samples. The measurements were performed using a commercially available instrument (RheoSpectris C500+; Rheolution, Montreal, Quebec, Canada), which introduces shear motion into the small cylindrical tube that contains the sample and uses nondestructive high sensitivity displacement laser measurements at the surface to measure the resulting vibration of the sample. This instrument uses the physical principle of resonant dynamic response of a material confined in a cylindrical tube. As described in more detail previously (15,16), the resonance eigenmodes of the sample are related to its viscoelasticity. A combination of sequential vibration pulses of different central frequencies and spectral distributions are used to mechanically excite the sample in a wide frequency band. From the corresponding spectrum, a proprietary algorithm is employed to allow accurate shear storage and loss modulus measurements over a broad range of frequencies from 1 to 2000 Hz. This form of DMA, which is sometimes called high-frequency viscoelasatic spectroscopy, was performed for each mixture at frequencies of 10–250 Hz at 10-Hz increments approximately 1 h prior to MRE data acquisition. For each mixture at each frequency, five repeated measurements were made on each small cylindrical tube sample for a total of 10 measurements. The average of these 10 measurements was used in subsequent comparisons with MRE. Standard error was computed using the standard deviation and mean for each measurement across all PVC samples. For each mixture at each frequency, the magnitude of the complex shear modulus, storage modulus, and loss modulus in kPa were estimated for comparison with

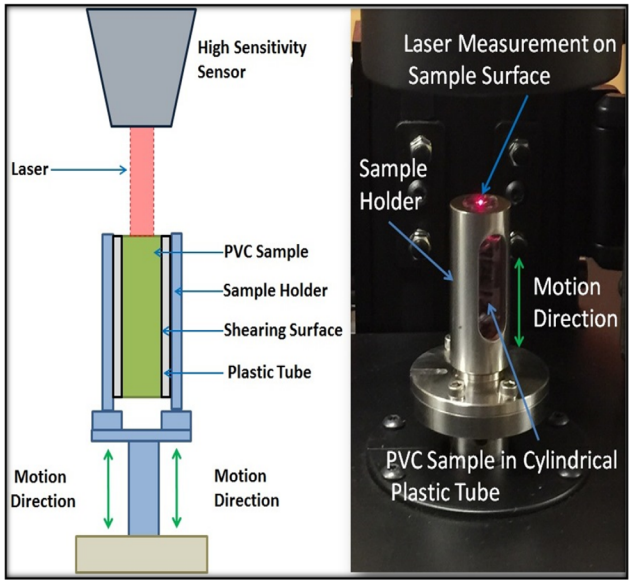

FIG. 1. Left: Schematic of the DMA instrument. Right: Photograph of the DMA instrument with the small cylindrical PVC sample in a plastic tube.

MRE measurements. Figure 1 (Left) shows the schematic of the DMA instrument used in this study, and Figure 1 (Right) shows the photograph of the RheoSpectris C500+ instrument with the PVC sample inside a plastic tube.

MRE Driving Frequencies

Comparison of 3D MRE and DMA stiffness was performed over a range of frequencies with comparable wavelengths across the eight different PVC phantoms to assess the influence of sample stiffness on the accuracy while holding the shear wavelength constant. From the obtained DMA storage modulus, MRE driving frequencies corresponding to nominal wavelengths of 1.1, 2.2, 3.3, 4.4, 5.5, and 6.6 across the diameter of each cylindrical phantom were estimated from the average DMA stiffness for each of the eight different PVC samples, interpolated to intermediate frequencies. These particular wavelengths were chosen to reduce resonance effects from driving at an integer number of wavelengths across the diameter of the cylindrical phantom. MRE was then performed on the PVC cylindrical phantoms at the prescribed frequencies across the eight phantoms. A table showing the actual driving frequencies, interpolated DMA stiffness, and other quantities for each case can be seen in the Supporting Information.

MRE Passive Driver Setup

Mechanical vibrations were introduced into the cylindrical phantom using a commercially available pneumatic active driver (Resoundant Inc., Rochester, Minnesota, USA) and a custom-made MRE passive driver. The cylindrical phantoms were placed on top of the passive driver (Fig. 2A), which was designed to cause the phantom to move uniformly in the axial direction of the cylinder. Figure 2B shows the sectional schematic of the custom-designed passive driver. Sound waves from the active

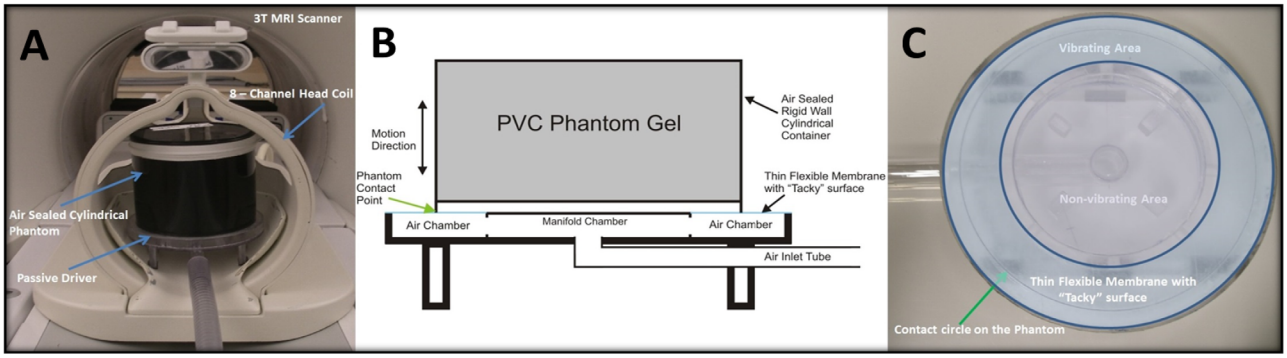

FIG. 2. (**A**) Photograph of the MRE cylindrical phantom. (**B**) Sectional schematic of the passive driver. The area within the manifold chamber is nonvibrating. The phantom contacts the driver only along the edges indicated by the green arrow and held in position by the adhesive surface in the blue region. (**C**) Photograph of the custom-built MRE passive driver. The vibrating area is shaded in blue, and the contact point with the phantom is a circular ring within the vibrating area represented by a pale black circle (indicated by the green arrow).

pneumatic driver entered the nonvibrating area in the manifold chamber, which has a hard plastic surface that enters the vibrating area. The passive driver has an adhesive surface that was achieved using a 1.15-mm-thick, two-sided adhesive tape in the vibrating region to eliminate unwanted right-to-left and superior–inferior drift during vibration and a circular marking to aid in phantom positioning (Fig. 2C). The driver only contacted the phantom around the bottom edge and not the entire bottom surface, as observed in the schematic in Figure 2B, reducing the amount of longitudinal wave energy introduced into the phantom to minimize phase wraps. This setup resulted in the side walls of the phantom becoming the source of shear wave generation and caused waves to propagate from the phantom edge to the center.

The diameter of the cylindrical phantom was 15.25 cm, and the desired ratio of the wavelength to the geometry represented by the nominal wavelengths of 1.1, 2.2, 3.3, 4.4, 5.5, and 6.6 wavelengths across the sample were achieved using the calculated vibration frequencies for each of the eight PVC samples. As an example, for PVC 50-50, the desired 2.2 wavelength-to-geometry ratio was obtained using a vibration frequency of 26.95 Hz, which resulted in 2.2 times the diameter of the cylindrical phantom (ie, 33.55 cm). These vibration frequencies for all eight PVC samples were estimated from the aforementioned DMA stiffness. The power settings for the active driver were determined and adjusted for each frequency across eight samples to produce approximately similar wave amplitudes as described later in the pilot study section.

MRE Image Acquisition

Imaging was performed on a 3.0T whole body MR imager (Optima MR450W; GE Healthcare, Milwaukee, Wisconsin, USA). The cylindrical phantom was placed on the custom-made passive driver and placed inside an eight-channel head coil (Fig. 2A). Imaging was performed in the coronal plane relative to the bore of the MRI scanner, which produced axial cross sections of the cylindrical phantom. A modified spin-echo echo planar imaging sequence was used for image acquisition at the specified vibration frequencies (Supporting Information) for each sample with the following acquisition parameters: number of shots = 2; number of excitations (NEX) = 8; repetition time = 877.9–1517.5 ms; echo time = 37–52 ms; field of view (FOV) = 32.0 cm; image matrix = 128 × 128; number of continuous 2.5-mm-thick coronal slices with 0 mm spacing = 11; number of motion-encoding gradient pairs = 1–3; and x, y, and z motion-encoding directions. Parallel imaging using sensitivity encoding (SENSE) reconstruction was accomplished with array spatial sensitivity encoding technique (ASSET) factor R = 2, and eight phase offsets spaced evenly over one vibration period were used. Data were acquired at 3-mm isotropic resolution. The vibration frequencies were matched with the motion-encoding frequency for frequencies greater than 80 Hz, and motion-encoding gradient mismatch was employed at lower frequencies to obtain reasonably lower echo times. Acquisitions were not performed for frequencies lower than 20 Hz due to the frequency response limitation of the active driver.

Pilot Study to Determine Power Levels

MRE image acquisition was performed on all eight samples using the aforementioned parameters except with the NEX = 1 as a pilot study. The primary purpose of this study was to determine the driver power levels needed to produce similar wave amplitudes with reasonable levels of phase wrap at each frequency across the eight samples. The power setting was manually set by starting at a high power level and reducing the driver power by 5% step by step until there were minimal or no phase wraps by visual inspection of the data at the scanner interface. These power settings were then used for the final MRE data acquisition. The vibration frequencies were chosen for the corresponding effective wavelengths for all eight PVC samples for MRE data acquisition.

MRE Image Analysis

The first temporal harmonic of the acquired wave images was calculated via temporal Fourier transform of the phase difference image series (3), and the curl operation

was applied using a 6 nearest neighbor kernel to the complex 3D displacement field to remove the effects of longitudinal waves that would otherwise produce artifacts in the inversion results. MRE DI was then performed as follows. First, the curled data were processed using a $3 \times 3 \times 3$ Romano (4) smoothing filter and 20 3D directional filters of order 4 with lower frequency cutoff at 0.5 cycles/field of view (FOV) and upper frequency cutoff at 40 cycles/FOV (17). Then three elastograms (one for each component of the curl) were calculated from the smoothed curl images using a 3D DI algorithm with a $3 \times 3 \times 3$ Laplacian 6 nearest neighbor kernel (3,18). A weighted average based on the squared amplitude of shear wave motion in each of the components of the curl was used to combine these elastograms into a single estimate for each slice. The final elastogram for each slice was smoothed using a $3 \times 3 \times 3$ cubic shaped spatial median filter to improve the regional homogeneity of tissue stiffness estimates. The direct inversion algorithm estimates the complex shear modulus with the storage modulus as the real part and the loss modulus as the imaginary part. These were then compared with DMA measured values for each of the PVC samples across different effective wavelengths.

MRE stiffness using 3D LFE was also performed on the curled first harmonic data to obtain the shear stiffness in kPa (3,19) using the standard default parameter settings for LFE (20). Shear stiffness is defined as the product of wave speed squared and density, where density is assumed to be that of water. DMA measured stiffness was converted to shear stiffness for comparison with LFE-derived shear stiffness.

The phantom was semi-automatically segmented from the magnitude images using a random walker segmentation algorithm (21). Four pixels were eroded along the slice-select direction and across the phantom diameter to reduce edge effects. The shear wave quality within the volume of interest was assessed using the octahedral shear strain signal-to-noise ratio (OSS-SNR), which has been shown to yield stable stiffness results above a threshold of 3 (22). The mean OSS-SNR was calculated from the curl-processed data for the selected volume, and mean MRE stiffness values were calculated using only voxels with OSS-SNR > 3 by excluding pixels with lower OSS-SNR values within the selected volume. MRE DI–derived stiffness and LFE-derived shear stiffness were then compared with DMA stiffness as the reference standard for the purposes of this study.

Effect of Spatial Resolution Compared with Theory

The results of DI can be affected by discretization error in the derivative estimation when the spatial resolution is low and there are insufficient pixels per wavelength (and thus the derivatives are estimated over a significant fraction of a wavelength). The closed-form expression for the underestimation error (ϵ_{max}) in a discrete Laplacian estimate of a pure complex sinusoid as a function of pixels/wavelength (N) for a [1 −2 1] central difference kernel is given by the following equation (see Supporting Information for derivation):

Table 1
Effective Wavelength (λ_{eff}), Corresponding Pixels per Wavelength, and Percentage Error for Discrete Laplacian Estimate

λ_{eff}	Pixels/ Wavelength	Discrete Laplacian Error %
1.1	55.45	0.11
2.2	27.73	0.42
3.3	18.48	1.01
4.4	13.86	1.67
5.5	11.09	2.69
6.6	9.24	4.00

$$\varepsilon_{max} = |1 - 0.5\left(\frac{N}{\pi}\right)^2\left[1 - \cos\left(\frac{2\pi}{N}\right)\right]|. \quad [1]$$

In this study, the 6.6 wavelength/diameter acquisitions had 9.2 pixels/wavelength (N), which should result in an overestimation of stiffness of about 4% using Equation [1]. This error estimate does not take into account the discretization error introduced by the curl processing, which is more difficult to analyze. Table 1 shows the expected % discrete Laplacian error for all the six different effective wavelengths (λ_{eff}). Papazoglou et al. (23) also analyzed Laplacian discretization error; for 9.2 pixels/wavelength, they predict an overestimation of 8%, but their analysis was based on a larger central difference scheme, using a [1 0 -2 0 1] kernel.

Statistical Analysis

The purpose of this study was to compare 3D MRE results with those of DMA under circumstances where the MRE acquisition was sufficient to allow accurate inversions. For this purpose, careful judgment was made to include only the datasets that had both adequate spatial resolution and adequate SNR. First, wave data with discrete Laplacian errors more than 3% were excluded from the statistical analysis to avoid overestimation bias. For this reason, the samples with 6.6 waves across the dimension of the cylindrical phantom were compared separately to analyze the overestimation resulting from the discretization error. Second, MRE data across all eight PVC samples with inadequate signal, defined as a mean OSS-SNR ≤ 3, were excluded from the analysis, because it has been reported that stable stiffness estimates can only be achieved above this threshold (22), and low SNR is known to cause MRE inversion algorithms to underestimate stiffness (15). Of the remaining samples, consistency between MRE and DMA was measured with intraclass correlation coefficient (ICC) using a one-way random effects model (24) separately for DI complex shear modulus, storage modulus, and loss modulus and also for LFE shear stiffness. Analysis was performed using SAS statistical software version 9.4 (SAS Institute Inc., Cary, North Carolina, USA).

RESULTS

DMA results showed that the eight PVC samples had stiffnesses in the range of 3−23 kPa. The average standard error across all the PVC samples based on the 10 measurements for each frequency was 4.75%. Supporting

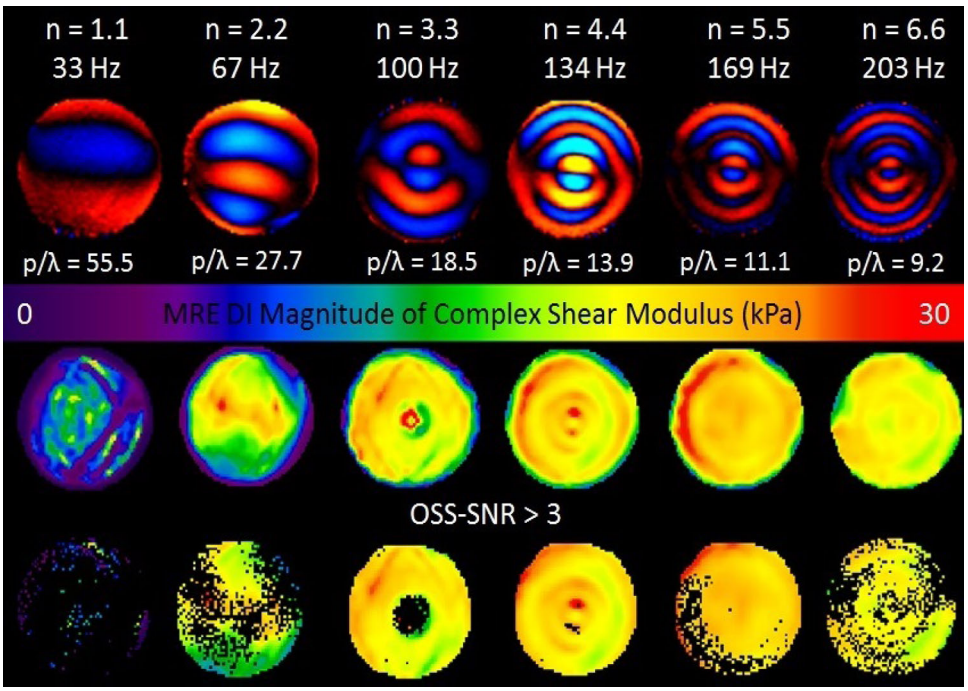

FIG. 3. Representative example of a PVC 95-05 sample. Top row: Effective wavelength n across the phantom diameter. Second row: Corresponding driving frequencies. Third row: X-component of the curled wave images of the center slice. Fourth row: Number of pixels per wavelength (p/λ). Fifth row: Color scale for the MRE DI magnitude of complex shear modulus in kPa. Sixth row: Elastograms from DI. Seventh row: Elastograms with pixels having OSS-SNR $>$ 3 used to calculate the mean MRE DI magnitude of complex shear modulus.

Tables S1–S8 show the effective wavelength (λ_{eff}); corresponding number of pixels per wavelength; driving frequency for each effective wavelength; magnitude of the complex modulus, storage modulus, and loss modulus for DMA and MRE DI; LFE shear stiffness; average OSS-SNR values; and the percentage of pixels with OSS-SNR $>$3 in the included volume for each PVC sample. Supporting Tables S1–S8 correspond to PVC 50-50, PVC 60-40, and so forth up to PVC 95-05, respectively. Figure 3 shows a representative example of the X-component of the curled data, the corresponding elastograms, and a map of the voxels with OSS-SNR $>$ 3 for wavelengths 1.1, 2.2, 3.3, 4.4, 5.5, and 6.6 for PVC 95-05. DMA testing revealed that this sample had a magnitude of complex shear modulus between 3 and 23 kPa for the frequency range 10–250 Hz. Figure 4 shows the X-component of the curled data for 4.4 effective wavelengths for all eight PVC samples with their associated frequencies of vibration.

Of the 48 MRE acquisitions, 27 were included in the comparison with DMA. Eight data points were excluded because they did not have sufficient spatial resolution (all of the 6.6 wavelength acquisitions). Eleven were excluded

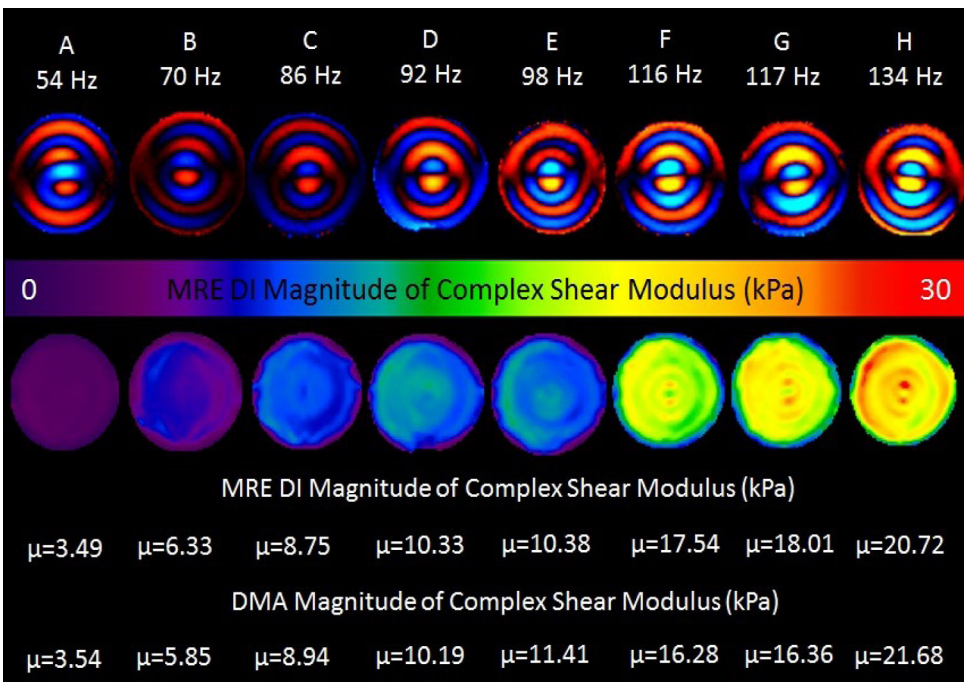

FIG. 4. Data for effective wavelength n = 4.4 across the diameter of the cylindrical phantom. Top row: The letters A–H represent the softest mixture (50% PVC 50% softener) on the left (A) to the stiffest mixture (95% PVC and 5% softener) on the right (H). Second row: Corresponding driving frequencies. Third row: X-component of the curled wave images of the center slice. Fourth row: Color scale for the MRE DI magnitude of complex shear modulus in kPa. Fifth row: Elastograms from DI. Sixth row: Mean MRE DI magnitude of complex shear modulus from pixels with OSS-SNR $>$ 3 in the included volume. Seventh row: DMA magnitude of complex shear modulus.

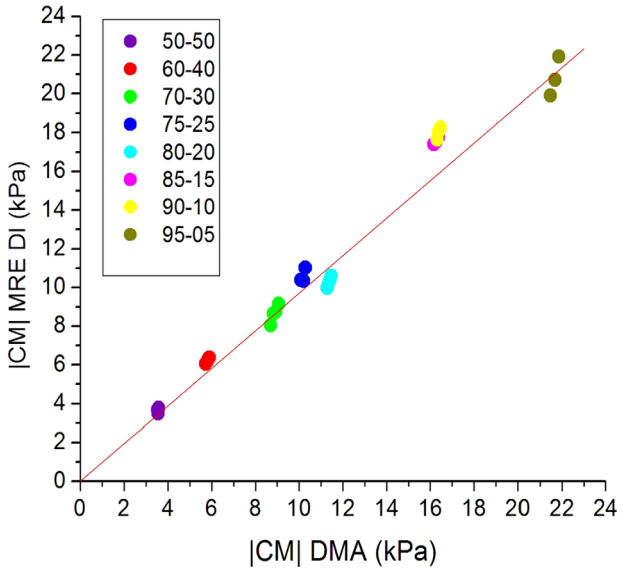

FIG. 5. Plot of DMA versus MRE DI magnitude of the complex modulus. The red solid line is the line of unity. ICC = 0.99 (95% CI = 0.97–0.99).

because the samples had a mean OSS-SNR $\leq$ 3 (all eight of the 1.1 wavelength acquisitions and three of the 2.2 wavelength acquisitions). Of the 27 included MRE/DMA comparisons, consistency with the magnitude of complex shear modulus was exceptionally high, with ICC = 0.99 (95% confidence interval [CI] = 0.97–0.99). Figure 5 shows the plot between MRE DI and the interpolated DMA stiffness (magnitude of the complex shear modulus) values across all frequencies for these data sets.

Consistency of the storage modulus estimated from MRE DI stiffness and DMA was also excellent, similar to the ICC estimation for the magnitude of the complex shear modulus with ICC = 0.99 (95% CI = 0.97–0.99). Figure 6 shows the plot between MRE DI and the DMA storage modulus values in kPa across all frequencies for these data sets.

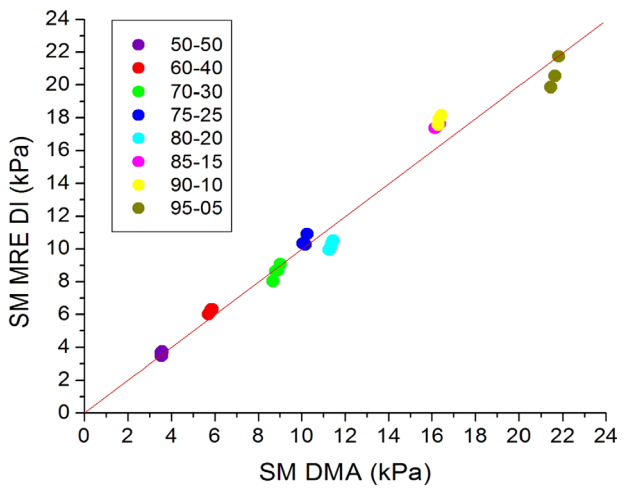

FIG. 6. Plot of DMA versus MRE DI storage modulus. The dotted line is the line of unity. ICC = 0.99 (95% CI = 0.97–0.99).

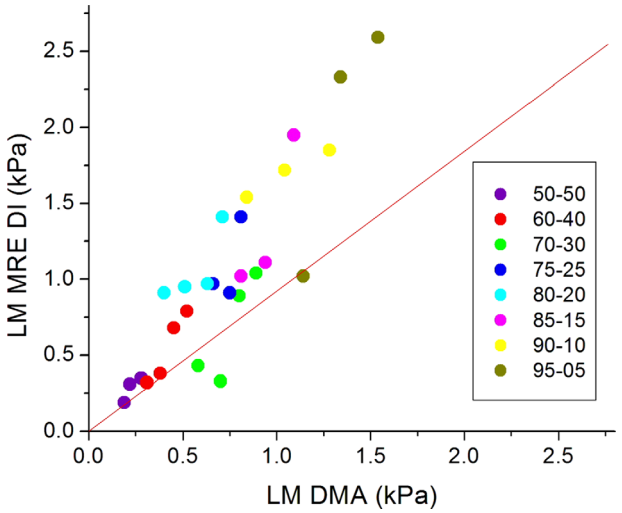

FIG. 7. Plot of DMA versus MRE DI loss modulus. The dotted line is the line of unity. ICC = 0.61 (95% CI = 0.31–0.80).

Consistency of the loss modulus estimated from MRE DI stiffness and DMA was lower with ICC = 0.61 (95% CI = 0.31–0.80). Figure 7 shows the plot between MRE DI and the DMA loss modulus values in kPa across all frequencies for these data sets with MRE overestimating loss modulus compared to DMA.

Consistency of the shear stiffness estimated using 3D LFE and DMA was also excellent, similar to the ICC estimation for the magnitude of the complex shear modulus with ICC = 0.99 (95% CI = 0.97–0.99). Figure 8 shows the plot between MRE LFE and DMA shear stiffness in kPa across all frequencies for these data sets.

The comparison results for 6.6 waves per dimension acquisitions are shown in Table 2. MRE overestimated stiffness compared with DMA by an average value of approximately 7.6% overall across the eight PVC samples. Only one data point for PVC 80-20 had an underestimated MRE DI stiffness. Overall, the results compared

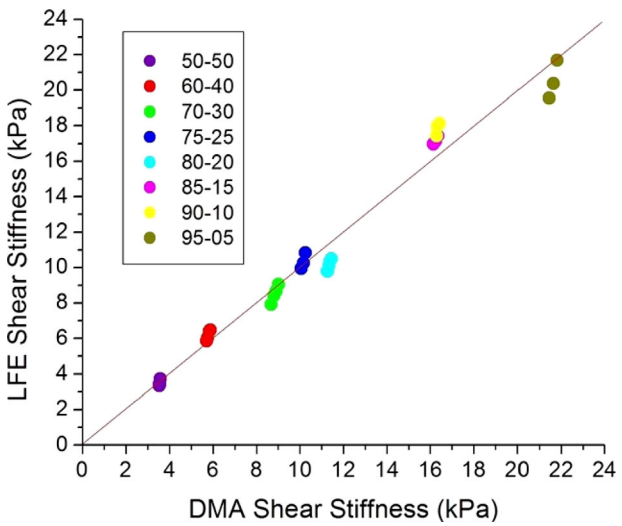

FIG. 8. Plot of DMA versus MRE LFE shear stiffness. The dotted line is the line of unity. ICC = 0.99 (95% CI = 0.97–0.99).

Table 2
Driving Frequency, Magnitude of the Complex Shear Modulus (|CM|) for DMA and MRE DI Estimate, MRE LFE Shear Stiffness, Average OSS-SNR for the Included Volume, Percentage of Pixels With OSS-SNR > 3 for All 8 PVC Samples and Percent Difference ((MRE DI − DMA)/DMA) Between MRE DI and DMA Estimates and LFE Shear Stiffness Estimates for Eight PVC Samples

PVC Sample	Frequency (Hz)	DMA|CM| (kPa)	MRE DI|CM| (kPa)	MRE LFE (kPa)	Average OSS-SNR	% pixels with OSS-SNR > 3	DI % Difference	LFE % Difference
50-50	81.96	3.59	3.95	3.89	22.65	100	10.03	8.36
60-40	105.09	5.92	6.56	6.47	18.22	100	10.82	9.29
70-30	130.89	9.13	9.60	9.42	16.93	100	5.15	3.18
75-25	139.17	10.37	11.64	11.57	8.41	99	12.25	11.57
80-20	147.06	11.51	11.20	11.11	26.73	100	−2.69	−3.47
85-15	176.29	16.47	18.05	17.95	6.43	93	9.60	8.98
90-10	175.76	16.58	18.53	18.52	4.73	80	12.44	11.71
95-05	203.24	22.05	22.74	22.44	4.03	70	3.13	1.77

Data are for effective wavelength (λ_{eff}) = 6.6 with a corresponding pixels per wavelength of 9.24.

well with the predicted values of 4% overestimation for our kernel size.

DISCUSSION

This is the first study to systematically study the quantitative accuracy of MRE stiffness using a material testing reference standard across a wide range of vibration frequencies without extrapolation. In this study, we have shown that 3D MRE DI and LFE measurements show excellent consistency with DMA measurements when studying samples with adequate number of pixels per wavelength and mean OSS_SNR (after the curl operation) > 3 over a wide range of sample stiffness.

This study used a wide range of matched DMA and MRE driving frequencies that ranged from 20 to 205 Hz. Earlier generations of DMA devices generally could only report low frequencies, typically from 1 to 100 Hz, or used custom-built mechanical testing devices that could reach higher frequencies but were not commercially available (6–11). Also, many previous studies used DMA instruments that required at least 10% precompression of the samples to avoid sample slipping. The applied precompression stresses the samples that affect the resulting DMA stiffness, and reproducibility is also a challenge under such circumstances. These issues are addressed with the DMA instrument used in this study, which does not require precompression for sample holding and can directly acquire data at higher frequencies. This has enabled a more robust and direct comparison of MRE measurements with DMA.

This study also applied statistical analysis to study the accuracy of MRE measurements with 3D processing by comparing it with DMA stiffness as a reference standard. One prior study reported correlation comparisons using 2D MRE, but there were no matched frequency comparisons between MRE and DMA, because DMA was performed from 10 to 50 Hz and MRE was performed from 100 to 200 Hz, and only average estimates were statistically compared (10). In the current study, many different batches of PVC phantoms with varying stiffness and matched MRE and DMA frequencies allowed systematic testing and comparisons and statistical analysis between MRE and DMA results.

The PVC phantoms used in this study were almost elastic, with very low loss modulus, so that the magnitude of the complex shear modulus, storage modulus, and shear stiffness (wave speed squared multiplied by density) are essentially identical. The ICC for the magnitude of the complex shear modulus and the storage modulus were very high (0.99), which shows excellent consistency between MRE and DMA. The ICC was much lower for the loss modulus (0.61), and MRE significantly overestimated the loss modulus relative to DMA, implying either a systematic bias in the DI algorithm or an error in the DMA measurements or both. Future comparisons with more viscoelastic phantom materials may provide more insight into this issue.

This study evaluated the accuracy of MRE over a wide range of stiffnesses and showed that 3D MRE provided accurate answers across the full range of stiffnesses tested as long as the criteria of adequate spatial resolution and SNR criteria were met. The 6.6 wave acquisitions were expected to have discretization errors of approximately 4% in calculating the Laplacian. The results indicate an approximate 7.6% overestimation by the MRE-derived stiffness, showing the importance of having sufficient spatial resolution to obtain accurate MRE stiffness. Similarly, the data sets with inadequate SNR (mean OSS-SNR < 3; the 1.1 and some of the 2.2 wave acquisitions) showed very strong underestimates of stiffness, as expected, showing the importance of adequate SNR. This emphasizes the importance of choosing the proper driving frequency for MRE to obtain both sufficient spatial resolution and adequate OSS-SNR.

There are several factors in the study design that may limit the generalization of the results. The first is that only data sets with adequate spatial resolution and sufficient signal based on OSS-SNR were analyzed for comparison between MRE DI, MRE LFE and DMA-derived stiffness. This approach was taken to perform a comparison between MRE and DMA under adequate conditions for MRE. Therefore, caution should be taken in generalizing these results if these conditions are not true, and it is often challenging to meet these conditions in some clinical applications of MRE.

Second, the phantom design lent itself to the generation of reflections. Both the enclosed cylindrical phantom and the choice of PVC as the medium (which has less damping than biologic tissues) encourage reflections, and for all samples, vibration frequencies were close to resonance. In addition, driving from the bottom of the

phantom with the energy transmitted to the sides of the cylinder created more bulk motion and reflections than would have been created by directly applying shear motion to the surface of the gels. However, PVC curing forms a meniscus on the surface of the gel that varies in dimension across different PVC samples, which would yield varying contact with the passive driver. Because uniform driving was critical to this study, it was elected to tolerate increased reflections and bulk motion rather than variable passive driver contact.

Third, the PVC gel yielded poor MR signal, and in particular the 1.1 wave acquisitions resulted in very low OSS-SNR despite using an NEX of 8 to boost the MR signal. Use of a phantom material with higher MR signal might have provided more data points for comparison.

Fourth, the MRE processing of the wave data used a fixed (and very small) kernel size for the DI algorithm to match some imaging scenarios, while one would typically use much larger kernels to derive a mean stiffness for a homogeneous phantom.

Fifth, the PVC phantoms used in this study were almost elastic, with very low loss modulus, but a systematic bias was observed in the loss modulus results. The cause of this bias remains under investigation. Because soft tissue is more viscoelastic, this weakens the validation of MRE with respect to soft tissue. However, the storage modulus results, with an ICC of 0.99, are unaffected by this bias, and the magnitude of the complex shear modulus and shear stiffness results will be affected only slightly except for materials with extremely high ratios of loss modulus to shear modulus.

Finally, the DMA instrument that was used as a reference standard in this study could have possible intrinsic errors in stiffness estimation that could have an effect on our study. However, the average standard error across all measurements was 4.75% implying highly reliable measurements. Based on these results, the authors believe that the limitation from the errors from DMA measurements in this study is minimal.

CONCLUSIONS

This study has studied the accuracy of 3D quantitative MRE by comparing directly with DMA measurements over a wide range of stiffnesses from 3 to 23 kPa and frequencies from 20 to 205 Hz. There was excellent consistency between MRE and DMA results for samples with OSS-SNR > 3, with an ICC value of 0.99. Samples with too low a spatial resolution showed an overestimation in stiffness, and samples with too low an SNR showed an underestimate of stiffness, both in accordance with theory. The results indicate that MRE data with adequate spatial resolution and SNR can yield accurate MRE stiffness values over a wide range of stiffnesses and frequencies.

ACKNOWLEDGMENTS

We thank Rickey Carter for performing the statistical analysis for the study.

REFERENCES

1. Muthupillai R, Lomas DJ, Rossman PJ, Greenleaf JF, Manduca A, Ehman RL. Magnetic resonance elastography by direct visualization of propagating acoustic strain waves. Science 1995;269:1854–1857.
2. Mariappan YK, Glaser KJ, Ehman RL. Magnetic resonance elastography: a review. Clin Anat 2010;23:497–511.
3. Manduca A, Oliphant TE, Dresner MA, Mahowald JL, Kruse SA, Amromin E, Felmlee JP, Greenleaf JF, Ehman RL. Magnetic resonance elastography: non-invasive mapping of tissue elasticity. Med Image Anal 2001;5:237–254.
4. Glaser KJ, Manduca A, Ehman RL. Review of MR elastography applications and recent developments. J Magn Reson Imaging 2012;36:757–774.
5. Hamhaber U, Grieshaber FA, Nagel JH, Klose U. Comparison of quantitative shear wave MR-elastography with mechanical compression tests. Magn Reson Med 2003;49:71–77.
6. Perreard IM, Pattison AJ, Doyley M, McGarry MD, Barani Z, Van Houten EE, Weaver JB, Paulsen KD. Effects of frequency- and direction-dependent elastic materials on linearly elastic MRE image reconstructions. Phys Med Biol 2010;55:6801–6815.
7. Doyley MM, Perreard I, Patterson AJ, Weaver JB, Paulsen KM. The performance of steady-state harmonic magnetic resonance elastography when applied to viscoelastic materials. Med Phys 2010;37:3970–3979.
8. Okamoto RJ, Clayton EH, Bayly PV. Viscoelastic properties of soft gels: comparison of magnetic resonance elastography and dynamic shear testing in the shear wave regime. Phys Med Biol 2011;56:6379–6400.
9. Vappou J, Breton E, Choquet P, Goetz C, Willinger R, Constantinesco A. Magnetic resonance elastography compared with rotational rheometry for in vitro brain tissue viscoelasticity measurement. MAGMA 2007;20:273–278.
10. Ringleb SI, Chen Q, Lake DS, Manduca A, Ehman RL, An KN. Quantitative shear wave magnetic resonance elastography: comparison to a dynamic shear material test. Magn Reson Med 2005;53:1197–1201.
11. Chen Q, Ringleb SI, Hulshizer T, An KN. Identification of the testing parameters in high frequency dynamic shear measurement on agarose gels. J Biomech 2005;38:959–963.
12. Sinkus R, Tanter M, Xydeas T, Catheline S, Bercoff J, Fink M. Viscoelastic shear properties of in vivo breast lesions measured by MR elastography. Magn Reson Imaging 2005;23:159–165.
13. Braun J, Guo J, Lutzkendorf R, Stadler J, Papazoglou S, Hirsch S, Sack I, Bernarding J. High-resolution mechanical imaging of the human brain by three-dimensional multifrequency magnetic resonance elastography at 7T. Neuroimage 2014;90:308–314.
14. Oliphant TE, Manduca A, Ehman RL, Greenleaf JF. Complex-valued stiffness reconstruction for magnetic resonance elastography by algebraic inversion of the differential equation. Magn Reson Med 2001;45:299–310.
15. Hadj Henni A, Schmitt C, Tremblay ME, Hamdine M, Heuzey MC, Carreau P, Cloutier G. Hyper-frequency viscoelastic spectroscopy of biomaterials. J Mech Behav Biomed Mater 2011;4:1115–1122.
16. Henni AH, Schmitt C, Cloutier G. Shear wave induced resonance elastography of soft heterogeneous media. J Biomech 2010;43:1488–1493.
17. Manduca A, Lake DS, Kruse SA, Ehman RL. Spatio-temporal directional filtering for improved inversion of MR elastography images. Med Image Anal 2003;7:465–473.
18. Murphy MC, Huston J 3rd, Jack CR Jr, Glaser KJ, Senjem ML, Chen J, Manduca A, Felmlee JP, Ehman RL. Measuring the characteristic topography of brain stiffness with magnetic resonance elastography. PLoS One 2013;8:e81668.
19. Manduca A, Muthupillai R, Rossman PJ, Greenleaf JF, Ehman RL. Local Wavelength Estimation for Magnetic Resonance Elastography. In Proceedings of the 3rd IEEE International Conference on Image Processing, Lausanne, Switzerland, 1996. pp. 527–530.
20. Grimm RC, Lake DS, Manduca A, Ehman RL. MRE/Wave. Mayo Clinic. http://mayoresearch.mayo.edu/mayo/research/ehman_lab. July 1, 2006. Accessed August 15, 2015.
21. Grady L. Random walks for image segmentation. IEEE Trans Pattern Anal Mach Intell 2006;28:1768–1783.

22. McGarry MD, Van Houten EE, Perrinez PR, Pattison AJ, Weaver JB, Paulsen KD. An octahedral shear strain-based measure of SNR for 3D MR elastography. Phys Med Biol 2011;56:N153–N164.
23. Papazoglou S, Hamhaber U, Braun J, Sack I. Algebraic Helmholtz inversion in planar magnetic resonance elastography. Phys Med Biol 2008;53:3147–3158.
24. Shrout PE, Fleiss JL. Intraclass correlations: uses in assessing rater reliability. Psychol Bull 1979;86:420–428.

SUPPORTING INFORMATION

Additional Supporting Information may be found in the online version of this article.

Table S1. Effective wavelength (λ_{eff}); corresponding pixels per wavelength; driving frequency; magnitude of the complex shear modulus (|CM|), storage modulus (SM), and loss modulus (LM) from DMA; magnitude of the complex shear modulus (|CM|), storage modulus (SM), and loss modulus (SM) from MRE DI estimate; average OSS-SNR for the included volume; and percentage of pixels with OSS-SNR $>$ 3 for PVC 50-50.

Table S2. Effective wavelength (λ_{eff}); corresponding pixels per wavelength; driving frequency; magnitude of the complex shear modulus (|CM|), storage modulus (SM). and loss modulus (LM) from DMA; magnitude of the complex shear modulus (|CM|), storage modulus (SM), and loss modulus (SM) from MRE DI estimate; average OSS-SNR for the included volume; and percentage of pixels with OSS-SNR $>$ 3 for PVC 60-40.

Table S3. Effective wavelength (λ_{eff}); corresponding pixels per wavelength; driving frequency; magnitude of the complex shear modulus (|CM|), storage modulus (SM), and loss modulus (LM) from DMA; magnitude of the complex shear modulus (|CM|), storage modulus (SM), and loss modulus (SM) from MRE DI estimate; average OSS-SNR for the included volume; and percentage of pixels with OSS-SNR $>$ 3 for PVC 70-30.

Table S4. Effective wavelength (λ_{eff}); corresponding pixels per wavelength; driving frequency; magnitude of the complex shear modulus (|CM|), storage modulus (SM), and loss modulus (LM) from DMA; magnitude of the complex shear modulus (|CM|), storage modulus (SM), and loss modulus (SM) from MRE DI estimate; average OSS-SNR for the included volume; and percentage of pixels with OSS-SNR $>$ 3 for PVC 75-25.

Table S5. Effective wavelength (λ_{eff}); corresponding pixels per wavelength; driving frequency; magnitude of the complex shear modulus (|CM|), storage modulus (SM), and loss modulus (LM) from DMA; magnitude of the complex shear modulus (|CM|), storage modulus (SM), and loss modulus (SM) from MRE DI estimate; average OSS-SNR for the included volume; and percentage of pixels with OSS-SNR $>$ 3 for PVC 80-20.

Table S6. Effective wavelength (λ_{eff}); corresponding pixels per wavelength; driving frequency; magnitude of the complex shear modulus (|CM|), storage modulus (SM), and loss modulus (LM) from DMA; magnitude of the complex shear modulus (|CM|), storage modulus (SM), and loss modulus (SM) from MRE DI estimate; average OSS-SNR for the included volume; and percentage of pixels with OSS-SNR $>$ 3 for PVC 85-15.

Table S7. Effective wavelength (λ_{eff}); corresponding pixels per wavelength; driving frequency; magnitude of the complex shear modulus (|CM|), storage modulus (SM), and loss modulus (LM) from DMA; magnitude of the complex shear modulus (|CM|), storage modulus (SM), and loss modulus (SM) from MRE DI estimate; average OSS-SNR for the included volume; and percentage of pixels with OSS-SNR $>$ 3 for PVC 90-10.

Table S8. Effective wavelength (λ_{eff}); corresponding pixels per wavelength; driving frequency; magnitude of the complex shear modulus (|CM|), storage modulus (SM), and loss modulus (LM) from DMA; magnitude of the complex shear modulus (|CM|), storage modulus (SM), and loss modulus (SM) from MRE DI estimate; average OSS-SNR for the included volume; and percentage of pixels with OSS-SNR $>$ 3 for PVC 95-05.